catalysts

MDPI

Article

Cu and Cu-Fe Bi-Metal Nanoparticles Encapsulated in Hollow S-1 Zeolite for Reverse Water Gas Shift Reaction

Rui Hu, Tianye Wang, Hongwei Li *, Yuan Zhu, Yifan Wang, Fuli Wen, Enhui Xing, Yu Wu and Zhijian Da *

Institute of Petroleum Processing, Sinopec, Beijing 100083, China; wangtianye.ripp@sinopec.com (T.W.); wenfuli.ripp@sinopec.com (F.W.); xingeh.ripp@sinopec.com (E.X.); wuyu.ripp@sinopec.com (Y.W.)
* Correspondence: lihongwei.ripp@sinopec.com (H.L.); dazhijian.ripp@sinopec.com (Z.D.)

Abstract: The hollow hierarchical structure Cu@S and $CuFe_{0.5}$@S catalysts were successfully synthesized through the "dissolution-recrystallization" (D-R) method for the reverse water gas shift reaction (RWGS). The encapsulated catalysts had a hierarchical porous structure and better dispersion of Cu particles than the Cu-S and $CuFe_{0.5}$-S samples prepared via the conventional impregnation method. Furthermore, $CuFe_{0.5}$-S and $CuFe_{0.5}$@S catalysts showed higher CO_2 conversion and 100% selectivity of CO at the entire temperature range investigated in this work compared to the monometallic catalysts Cu-S and Cu@S. Interestingly, the reaction activity of all the samples increased according to the sequence: $CuFe_{0.5}$@S > $CuFe_{0.5}$-S > Cu@S > Cu-S at 400–550 °C under atmospheric pressure. These results indicate that the higher dispersion of encapsulation structure and the enhanced surface basicity derived from the addition of Fe play crucial roles in enhancing the catalytic performance of Cu-based catalysts in the RWGS reaction.

Keywords: hollow zeolite; Cu catalysts; Cu-Fe bimetal; encapsulation; RWGS reaction

Citation: Hu, R.; Wang, T.; Li, H.; Zhu, Y.; Wang, Y.; Wen, F.; Xing, E.; Wu, Y.; Da, Z. Cu and Cu-Fe Bi-Metal Nanoparticles Encapsulated in Hollow S-1 Zeolite for Reverse Water Gas Shift Reaction. *Catalysts* **2023**, *13*, 1037. https://doi.org/10.3390/catal13071037

Academic Editor: Eun Duck Park

Received: 29 May 2023
Revised: 9 June 2023
Accepted: 10 June 2023
Published: 26 June 2023

1. Introduction

The capture, conversion and utilization of CO_2 have been popular issues which play important roles in reducing greenhouse gas (GHG) emissions for environmental protection and achieving carbon cycling for the development of the recycling economy [1,2]. One potential CO_2 utilization pathway is the reverse water gas shift (RWGS) reaction ($CO_2 + H_2 = CO + H_2O$), which contributes to the conversion of the highly stable CO_2 molecule into an active CO molecule. As the key building block, CO can be transformed into light olefins, long-chain hydrocarbons, methanol and other high-value-added oxygenates [3]. The RWGS reaction is an endothermic reaction that transforms CO_2 into CO at atmospheric pressure and high temperature (>300 °C) [4,5]. Taking into account the reaction pressure, there is no doubt that achieving efficient conversion of CO_2 at low pressure will be a considerable advantage. In addition, the RWGS reaction is a heterogeneous catalytic reaction. An ideal design of a catalyst system considers both excellent catalytic performance and fair cost to play an important role in large-scale CO_2 conversions. Among the many catalyst systems, Cu-based catalysts have been studied the most in CO_2 hydrogenation reactions for their low cost and optimal catalytic activity [6]. Jurovi'c et al. [7] reported that Cu-based catalysts are sensitive to their structural characteristics by establishing the exposed Cu sites and RWGS reaction rate. B.M. Weckhuysen et al. [8] have also revealed that the activity of Cu catalysts was related to increased metal dispersion, higher Cu^0: CuO ratios and adequate surface basicity sites. Moreover, deactivation is closely related to metal sintering under a high reaction temperature. In this regard, the optimization of the catalyst structure via adding textural promoters [9,10], such as Fe or Zn or confining the metal nanoparticles in inner channels or pores of porous supports, helps to resist aggregation resulting in the high stability of catalysts [11,12].

The metal@zeolite catalysts have attracted much interest due to their superior enhancement of the catalytic performance in many fields in recent years [13,14]. Wang et al. [10]

reported a maximum activiation selectivity of 45% over the hollow hierarchical S-1 zeolite encapsulated PtNi nanoparticle catalyst PtNi@S-1, synthesized by the dissolution recrystallization (D-R) method. The results showed that not only the selectivity of the products but also the stability of the PtNi@S-1 was significantly higher than that of the PtNi/S-1 catalyst synthesized via the conventional impregnation method. Kwok et al. [15] synthesized the Fe@h-ZSM-5 catalyst by the DR method and used it for the Fischer–Tropsch reaction. It was found that the Fe@h-ZSM-5 catalyst exhibited significant advantages, such as excellent activity, outstanding coking and a sinter-resistance ability over the Fe/ZSM-5. Ma et al. [16] researched the catalytic performance in dry reforming of methane with high loading and uniform Ni nanoparticles encapsulated in the Silicalite-1 zeolite of which the sizes of Ni NPs were maintained at ca.4–5 nm and the TOF was kept at 60 s^{-1} (800 °C) by increasing the Ni loading from 3% to 20%. The evolution results exhibited that the catalysts with various Ni loadings all exhibited high stability upon running for 150 h. In addition, Kang et al. [17] reported a sodium-modified rhodium nanoparticles embedded in the Silicalite-1 zeolite catalyst Na-Rh@S-1 and revealed that the catalyst Na-Rh@S-1 with the encapsulated structure exhibited a higher dispersion of Rh nanoparticles and more outstanding activity for the CO_2 hydrogenation to ethanol reaction.

Although metal@zeolite catalysts showed excellent catalytic performance in many fields, the research into Cu embedding in zeolites was relatively less than other transition metals. In addition, there have been rare reports related to Cu confined in the ZSM-5 zeolite catalysts for C1 chemistry, especially for RWGS reaction. Therefore, in this work, in order to adequately integrate the unique Cu-based catalyst for the RWGS reaction with the promoter effect of Fe and the confinement effect of metal@zeolite, the Cu and Cu-Fe bi-metal nanoparticles embedding in the hollow S-1 zeolite were prepared via the D-R method, which was denoted as Cu@S and $CuFe_{0.5}$@S. Meanwhile, the catalytic activity over different catalysts was investigated. The influence of the hollow encapsulated structure on the CO_2 conversion and CO selectivity were emphatically focused on.

2. Results and Discussion

2.1. Textural Characteristics and N_2 Physisorption

The pore structure properties of the parent S-1 zeolite and the catalysts were characterized with N_2-BET. As shown in Figure 1A, the parent S-1, Cu-S and $CuFe_{0.5}$-S all showed the same type of isotherms, which indicated that, the loading of active metals has little effect on the structure of the silicalite-1 zeolite. For Cu@S and $CuFe_{0.5}$@S, the type-IV isotherms with an H2 hysteresis loop, which consists of an abrupt step at around $P/P_0 = 0.45$, were characteristic of the cavitation phenomenon or pore-blocking effect [18,19]. This feature implies that there existed an ink-bottle pore system in the samples, which means that the zeolite has cavities connected to the outside through narrow channels (<4 nm) [19,20]. In addition, for all the samples, the steep increase in adsorption quantities and the hysteresis curves at high relative pressure $P/P_0 > 0.9$ demonstrated the existence of mesopores derived from the aggregation of zeolite crystals [21]. The NLDFT pore size distribution curves presented in Figure 1B further confirmed that the Cu@S and $CuFe_{0.5}$@S catalysts possessed a hierarchical porous structure, and the size of mesopores generated from TPAOH treatment was concentrated at 2~4 nm. Except for the parent S-1, Cu-S and $CuFe_{0.5}$-S samples, the catalysts Cu@S and $CuFe_{0.5}$@S mainly presented microporous structures and a small quantity of mesoporous structures can be observed at 2~4 nm, which were inter-crystalline mesopores generated by the aggregation of the zeolite crystals.

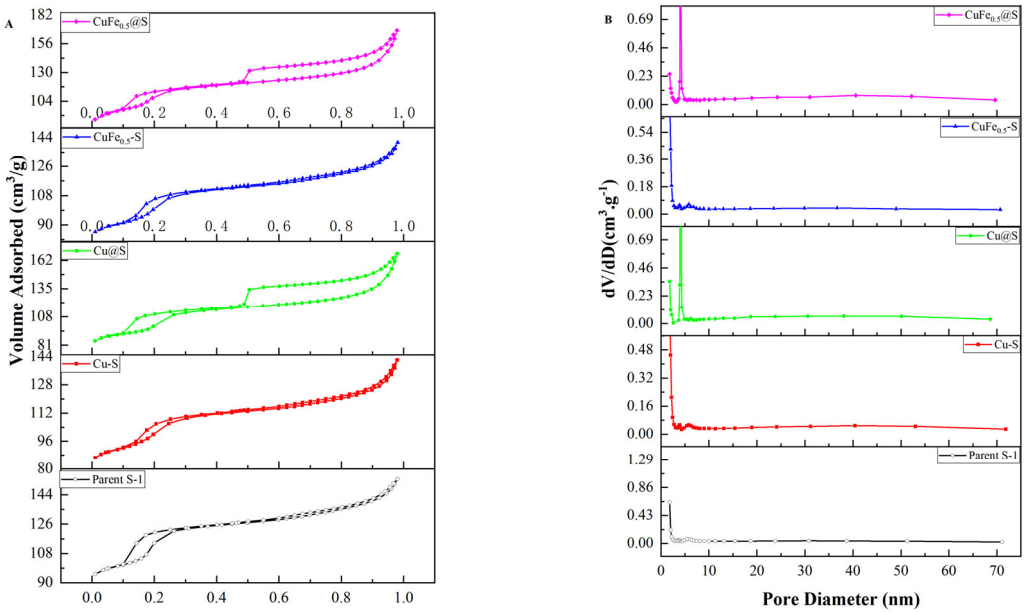

Figure 1. (**A**): N_2 absorption-desorption isotherm curves and (**B**): pore size distributions of all the samples.

The textural properties of all samples which were derived from the N_2-BET experiment were summarized in Table 1. It can be observed that the parent S-1 possessed the largest specific surface area (390.6 $m^2.g^{-1}$) and microporous specific surface area (356.2 $m^2.g^{-1}$). After impregnation, the specific surface and the total volume of Cu-S and $CuFe_{0.5}$-S decreased slightly since the metal deposited in the micropores and on the external surface of catalysts. In addition, the specific surface of Cu@S decreased by 1.67% compared to the Cu-S sample due to its smoother crystal surface caused by the recrystallization [22]. Compared to Cu-S, the Cu@S exhibited both a decrease (6.13%) in the microporous specific area and an increase (41.11%) in the external specific area, which suggests the formation of mesopores during the encapsulation process [20]. However, the specific area of $CuFe_{0.5}$@S increased by 8.41% compared to $CuFe_{0.5}$-S, which was contrary to the previous situation. It was speculated that the Fe originally deposited in the micropores and external surface entered the skeleton of zeolite during the TPAOH treatment process, which was consistent with the result that $CuFe_{0.5}$@S exhibited larger microporous (increased by 6.69%) and external specific areas (increased by 23.17%). These results further confirmed that Cu@S and $CuFe_{0.5}$@S possess a hierarchical porous structure, which were in agreement with the experimental results reported for hollow MFI zeolites [20,23,24].

Table 1. Textual Properties of Parent S-1 Zeolite and Series Catalysts.

Samples	S_{BET} [a] (m^2/g)	S_{micro} [b] (m^2/g)	$S_{meso/ext}$ [c] (m^2/g)	V_{total} [d] (cm^3/g)	V_{micro} [b] (cm^3/g)
Parent S-1	390.6	356.2	34.4	0.238	0.174
Cu-S	342.6	310.2	32.4	0.220	0.154
Cu@S	336.9	291.2	45.7	0.260	0.151
$CuFe_{0.5}$-S	340.6	305.1	35.5	0.218	0.152
$CuFe_{0.5}$@S	369.2	325.5	43.7	0.256	0.158

Notes: [a] Determined by the BET method; [b] Calculated by t-plot method; [c] Calculated using "S_{BET}-S_{micro}"; [d] Results Taken from the N_2 adsorbed at P/P_0 = 0.95.

2.2. XRD and TEM Experiments

The XRD data obtained for all samples are shown in Figure 2. All the samples exhibited characteristic diffraction peaks at 2θ = 7.96°, 8.82°, 23.08°, 23.97° and 24.43°corresponding

to the (011), (200), (501), (033) and (133) facets of the Silicalite-1 zeolite (PDF#44-969) [15]. To characterize the change in relative crystallinity, the 2θ = 22.5°~25°of the standard ZSM-5 sample was selected as reference, and the relative crystallinity of all the samples is calculated as follows and shown in Figure 2A. The parent S-1 presented a high relative crystallinity close to the standard sample. However, the other catalyst samples presented a lower crystallinity, indicating that some zeolite frameworks were destroyed during the process of loading metals. In addition, there was little change in the relative crystallinity among the different catalysts. A closer observation of the XRD patterns (Figure 2B) showed that all catalysts possessed the peaks at around 2θ = 35.5°, 38.7° and 48.8° which were consistent with the (002), (111) and (−202) facets of the CuO phase (PDF#89-5895). After that, the other two low-intensity peaks at 37.7° and 42.61°might be attributed to the Cu_2O phase (PDF#34-1354). No obvious diffraction peaks from iron oxide were observed due to the low content. The average size of CuO for all the samples was calculated based on the CuO (111) facet using Scherrer's equation. Therefore, the results of Cu crystal sizes for Cu-S, Cu@S, $CuFe_{0.5}$-S and $CuFe_{0.5}$@S are 22.6 nm, 17.6 nm, 23.2 nm and 21.7 nm, respectively, demonstrating that the catalyst encapsulated structures have lower particle sizes. Compared to Cu-S, the addition of Fe had no obvious effects on the CuO size. Nevertheless, it might be the association of Cu and Fe oxide during the encapsulation process, because $CuFe_{0.5}$@S displayed a larger particle size compared to Cu@S.

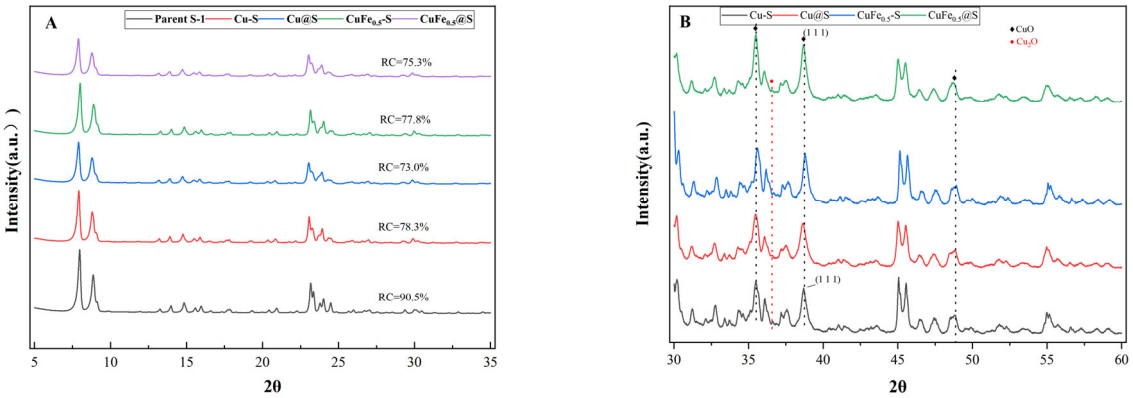

Figure 2. XRD patterns of parent S-1 zeolite and series catalysts: (**A**) the relative crystallinity; (**B**) the XRD phase.

Figure 3 shows the TEM micrographs obtained from the fresh catalysts. The images of Figure 3A–D, respectively, correspond to the Cu-S, $CuFe_{0.5}$-S, Cu@S and $CuFe_{0.5}$@S samples. Compared to the encapsulated structural catalysts, Cu-S and $CuFe_{0.5}$-S did not display visible metal oxide nanoparticles uniformly distributed on the zeolite frameworks, which might be attributed to aggregation of metal particles under the calcination process of the samples. Nevertheless, Cu@S and $CuFe_{0.5}$@S showed obvious uniform nanoparticles embedded in the cavity of the zeolite, which was consistent with the N_2-BET results. The CuO nanoparticle size of the Cu@S and $CuFe_{0.5}$@S were 12.83 nm and 17.7 nm, respectively, resulting from counting at least 80 particles of several TEM images, which were slightly smaller than the results (17.6 nm for Cu@S and 22.2 nm for $CuFe_{0.5}$@S) calculated via XRD. Additionally, the metal dispersion (D) was calculated from the equation $D = \frac{k}{d}$ according to the methodology proposed in [25] by using the relationship between the number of surface (n_s) and total (n_t) atoms. The coefficient k can be expressed via the equation [5] $k = \frac{M.n_s}{\rho.N_A}$, where M is the molar mass, ρ accounts for the density, N_A denotes Avogadro's number and d is the particle size. Based on the above equation, the dispersions for Cu-S, $CuFe_{0.5}$-S, Cu@S and $CuFe_{0.5}$@S were 7.96%, 7.74%, 14.63% and 10.38% which were summarized in Table 2. The chemical compositions of samples, analyzed by XRF and XPS, are also listed in Table 2. XPS is a surface technique with an analysis depth of <10 nm and XRF can analyze the bulk composition, therefore, XPS/XRF can be used to characterize the distribution

of Cu on the sample surface and inside the cavity of the zeolite [23,26]. By comparing the results of XPS/XRF, the encapsulated structural samples Cu@S and $CuFe_{0.5}$@S had smaller ratios than the Cu-S and $CuFe_{0.5}$-S samples, which further confirms the Cu species were successfully encapsulated into the S-1 zeolite. These results are consistent with the TEM images.

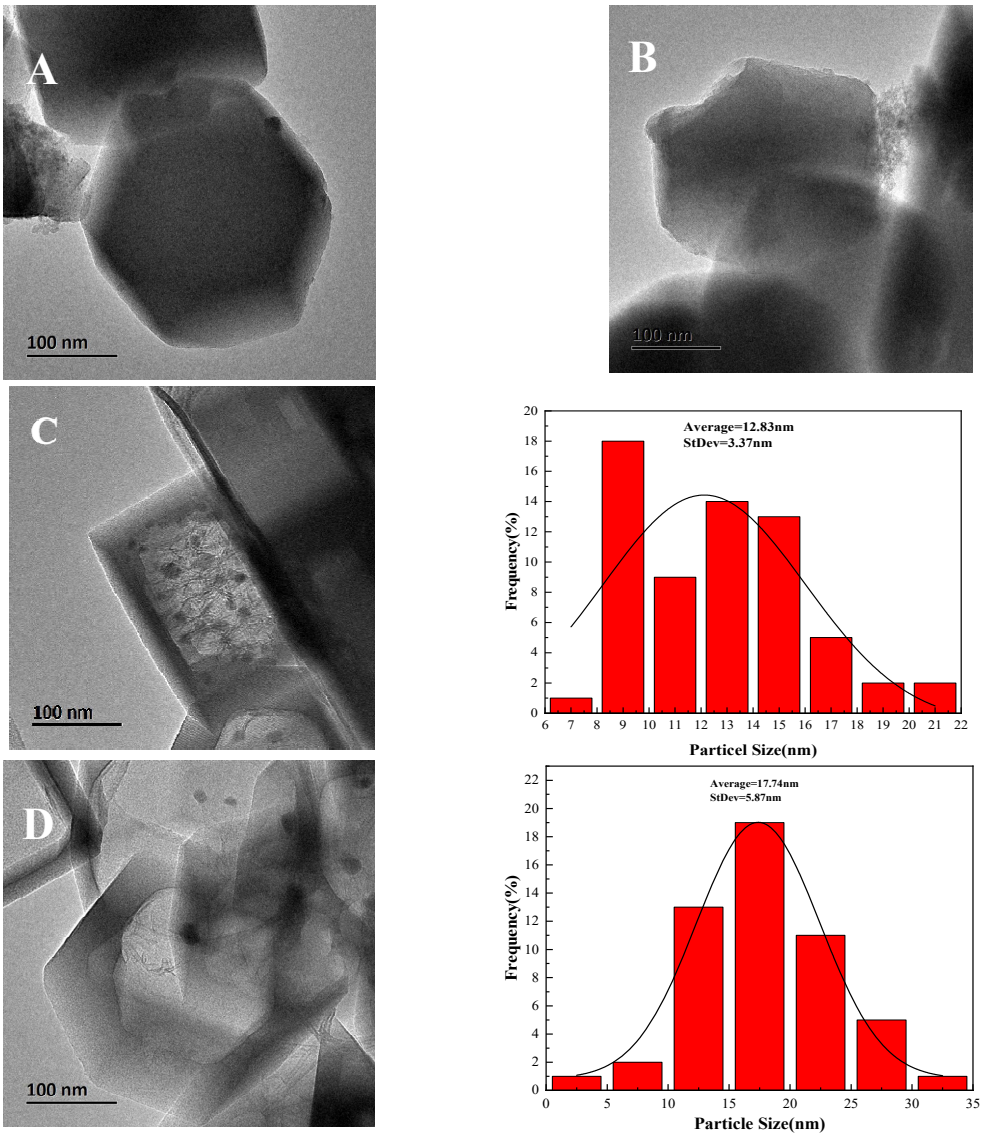

Figure 3. TEM images and particle distribution: (**A**) Cu-S, (**B**) $CuFe_{0.5}$-S, (**C**) Cu@S, (**D**): $CuFe_{0.5}$@S.

Table 2. Metal loading and Dispersion.

Samples	Metal loading [a]/%		Cu/Si [b]		XPS/XRF	d_{Cu} (nm)	D_{Cu} (%)
	Cu	Fe	XPS [c]	XRF			
Cu-S	5.16		0.032	0.052	0.62	22.6	7.96
Cu@S	5.64		0.021	0.058	0.36	12.83 ± 3.35	14.63
$CuFe_{0.5}$-S	5.26	0.53	0.048	0.054	0.89	23.2	7.74
$CuFe_{0.5}$@S	6.82	0.70	0.037	0.072	0.51	17.74 ± 5.87	10.38

Notes: [a] Calculated by XRF; [b] Molar ratio of Cu to Si; [c] Determined using $Cu/Si = (I_{Cu}/f_{Cu})/(I_{Si}/f_{Si})$, where I is the peak area of XPS and f is the atom sensitivity of factor. In this work, $f_{Cu} = 5.321$, $f_{Si} = 0.328$.

2.3. H_2-TPR and CO_2-TPD Experiments

The reducibility of different catalysts was exhibited in Figure 4A. All the samples present obvious reduction peaks near 200 °C, which could be ascribed to the characteristic peak of CuO. The difference was that the peaks of Cu@S and $CuFe_{0.5}$@S shifted to higher temperatures compared to Cu-S and $CuFe_{0.5}$@S, which might be due to the Metal-Si strong interaction resulting from the encapsulated structure catalysts that suppressed the reduction of the metal oxide [18,19]. Additionally, other reducibility peaks of Cu at higher temperatures could be attributed to the presence of highly dispersed Cu_2O species. For the Cu-Fe bi-metal catalysts, the peak between 300 °C and 400 °C is the reduction peak of FeO_x.

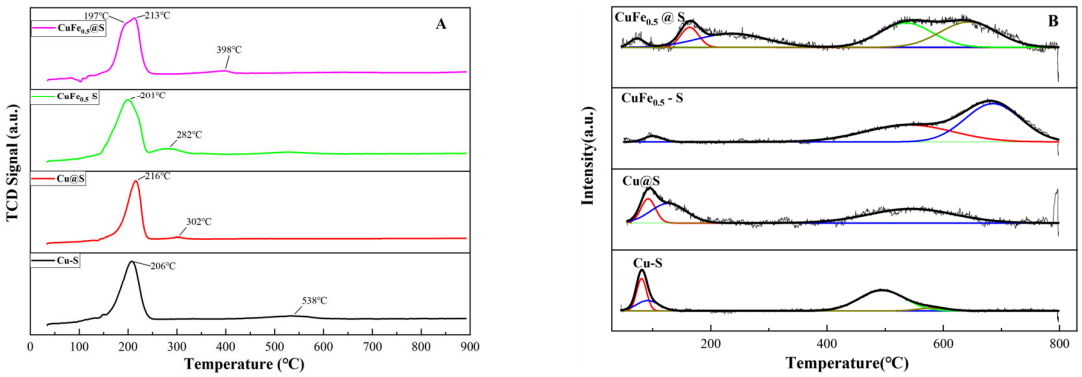

Figure 4. (**A**) H_2-TPR, (**B**) CO_2-TPD profiles of different catalysts.

CO_2-TPD profiles were utilized to underline the surface basic characteristics of catalysts by the temperature and intensity of the desorption peaks which were shown in Figure 4B. The temperature and intensity of the desorption peak underline the surface basic characteristics of catalysts. In general, a higher the desorbed temperature corresponds to a stronger basicity of the catalysts. For instance, the lower temperature (<150 °C), the moderate temperature (150~450 °C) and the higher temperature (>450 °C) could be, respectively, related to weak, moderate and strong basic sites in the samples [5]. The specific results of peak fitting by the deconvolution of curves based on a Gaussian function are summarized in Table 3. For the lower temperature peaks, it can be speculated that the peaks at below 100 °C should be attributed to the physisorption of the CO_2 molecule's interaction with the porous catalysts, which can be explained by the fact that the CO_2 hydrogenation reaction over Cu-based catalysts at low temperature has no activity. Compared Cu-S with Cu@S, the proportions of different types of basic sites were similar, which is the reason that the change of texture structure has little effect on the surface basicity of catalysts. However, introducing the Fe promoter changed the basicity of the catalyst, which can be seen from the increased number of strong basic sites in the CO_2-TPD results. Furthermore, compared to the $CuFe_{0.5}$-S catalyst, the $CuFe_{0.5}$@S sample exhibited superior amounts of moderate basic sites which were related to improved capacities of adsorbing and activating the highly stable CO_2 molecules and decomposition of intermediate species into reaction products achieving the RWGS reaction rate [5].

Table 3. The results of fitting peaks of different catalysts.

Samples	Weak		Moderate		Strong	
	Peak 1 /°C	Peak 2 /°C	Peak 3 /°C	Peak 4 /°C	Peak 5 /°C	Peak 6 /°C
Cu-S	81.07 (20.52%)	91.43 (14.52%)			494.52 (59.65%)	582.32 (5.31%)
Cu@S	92.30 (15.59%)	126.95 (30.69%)			545.29 (53.72%)	
$CuFe_{0.5}$-S		101.85 (2.89%)			540.58 (40.27%)	685.23 (56.84%)
$CuFe_{0.5}$@S	73.11 (2.92%)		163.69 (8.67%)	235.84 (22.74%)	535.59 (31.13%)	643.56 (34.54%)

Notes: The number in the bracket represents the percentage of area quantity.

2.4. CO_2 Hydrogenation Activity

Figure 5 shows the RWGS catalytic performance for catalysts with different configurations under the conditions of 17.8 L/h and H_2/CO_2 = 3/1. Figure 5A displays the generally increasing conversion of CO_2 as the temperature rises from 400 °C to 550 °C. Furthermore, the reaction activity of all the samples increased according to the sequence: $CuFe_{0.5}$@S > $CuFe_{0.5}$-S > Cu@S > Cu-S. Comparing the CO_2 conversion on Cu-S and Cu@S catalysts, it can be speculated that the higher Cu dispersion and hierarchical porous structure contributed to enhancing the catalytic performance resulting from the high activity of nanoparticles and better diffusion performance of the mesoporous structure. Surprisingly, the catalysts containing the Fe agent exhibited significantly better performance than the Cu-S and Cu@S samples in both the CO_2 conversion and CO selectivity (as shown in Figure 5B). In fact, the TOF values of Cu-S, $CuFe_{0.5}$-S, Cu@S and $CuFe_{0.5}$@S (3.68×10^{-3}, 5.17×10^{-3}, 1.79×10^{-3} and 3.13×10^{-3}, respectively) were estimated at the initial temperature of 400 °C. It can be inferred that the catalytic enhancement is related to the introduction of Fe, which is reported [5] to be associated with the presence of Cu-FeO_x domains with improved CO_2 dissociation abilities. CO_2-TPD results indicated that the increased surface basic sites are related to the Fe presence. Furthermore, it was reported [27] that the Cu-FeO_x interface contributed to achieving the RWGS reaction rates by increasing the electron density on Cu metal interfaces. The CO selectivity results displayed in Figure 5B demonstrated that the Cu-based catalyst has superior performance on the RWGS reaction than other the catalytic series, which the selectivity of Cu-S and Cu@S was 90.94% and 87.82% at 400 °C, respectively. These results further illustrated the advantage of samples containing FeO_x species over non-Fe Cu catalysts.

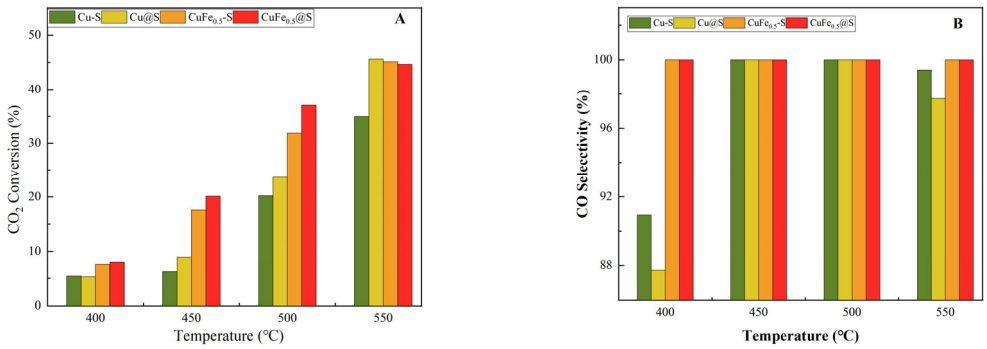

Figure 5. Catalytic performance for the samples at 17.8 L/h at H_2/CO_2 = 3/1: (**A**) Conversion of CO_2; (**B**) CO selectivity.

Overall, the Cu-based catalysts with hollow S-1 zeolite structure and Fe promoter indeed contributed to the RWGS reaction. The encapsulation structure has a better Cu dispersion and a better diffusion of molecules, which is related to the reaction activity. The incorporation of FeO_x species, either in co-impregnated or embedded in zeolite support, significantly enhances the transformation of CO_2 into a goal product which is attributed to the unique electronic effect and structure effect of Cu-FeO_x. In addition, the moderate surface basicity sites displayed in the CO_2-TPD results of $CuFe_{0.5}$@S further engaged the catalyst with a better catalytic performance over the entire temperature range.

In order to explore the stability of the Cu-based catalysts with different structures, the change in CO_2 conversion with time under the same experimental conditions was used as an indicator of the catalyst stability. The results are shown in Figure 6. With the extension of time, the CO_2 conversion of different catalysts was significantly different. The stability of Cu-S and $Cu_{0.5}$-S catalysts prepared by the impregnation method was lower than that of Cu @ S and $CuFe_{0.5}$-S catalysts encapsulated by the hierarchical porous zeolite during the whole evaluation period of 120 h. It fully showed that the confinement effect of the zeolite on the metal nanoparticles can effectively improve the stability of the catalysts. In addition, comparing the catalyst Cu-S with $CuFe_{0.5}$-S, it is not difficult to find that the

activity of $Cu_{0.5}$-S was significantly higher than that of Cu-S within 50 h before the reaction because the Fe promoter can improve the RWGS reaction activity of copper-based catalysts. In general, the stability of the encapsulated catalyst was better than that of the supported catalyst prepared by the impregnation method, which was consistent with the initial idea of the confinement effect of zeolite metal nanoparticles.

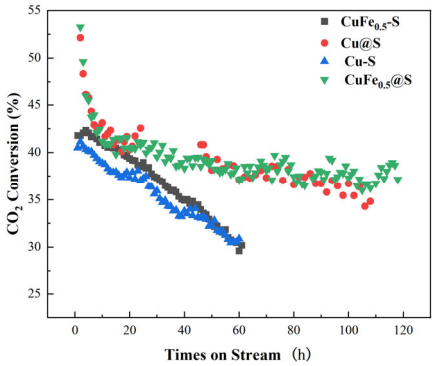

Figure 6. Conversion as a function of time on stream for different catalysts.Reaction conditions: 17.8 L/h, H_2/CO_2 = 3/1 and 550 °C.

3. Experimental Section

3.1. Materials

Tetrapropylammonium hydroxide solution (TPAOH, 25%), ethyl orthosilicate (TEOS, AR), $Cu(NO_3)_2$ $3H_2O$ (AR) and $Fe(NO_3)_3$ $9H_2O$ were purchased from Shanghai Aladdin Bio-Chem Technology Co., Ltd., Shanghai, China.

3.2. Catalysts Preparation

3.2.1. Synthesis Parent S-1 Zeolite

Silicalte-1 zeolite was synthesized by the clear solution method with the molar ratio of $1SiO_2$:0.3TPAOH:$37H_2O$. Typically, 10.00 g TEOS, 14.29 g TPAOH and 18.21 g deionized water were mixed in a 100 mL beaker under stirring at room temperature for 6 h. Then the above mixture was transferred to a 100 mL Teflon-lined steel autoclave for crystallization. After that, the product was obtained via centrifugation and dried overnight at 105 °C. Finally, the zeolite sample was calcined in a muffle furnace at 550 °C for 2 h to remove the organic template.

3.2.2. Preparation of Cu-S and $CuFe_{0.5}$-S Catalysts

Cu-S and $CuFe_{0.5}$-S catalysts were synthesized by an impregnation method. Briefly, the parent S-1 zeolite was impregnated with $Cu(NO_3)_2$ solution and $Cu(NO_3)_2$ -$Fe(NO_3)_3$ co-solution. After the impregnation process, the samples were dried at 105 °C for 12 h, and then calcined at 450 °C for 4 h. The obtained catalysts were named Cu-S-1 and $CuFe_{0.5}$-S-1, respectively. The ideal Cu, Fe loading was 5% and 0.5%, respectively.

3.2.3. Preparation of Cu@S and $CuFe_{0.5}$@S Catalysts

Cu@S and $CuFe_{0.5}$@S catalysts were synthesized by a dissolution-recrystallization (DR) method [18,20,28]. In brief, the as-prepared Cu-S-1 and $CuFe_{0.5}$-S catalysts were treated with TPAOH solution at 170 °C for 24 h and the molar ratio of SiO_2: TPAOH: H_2O was 1:0.25:22. After being cooled to room temperature, the products were recovered by centrifugation and washed at pH = 7.0 with deionized water. Then the samples were dried overnight at 105 °C and calcined at 450 °C for 4 h. The final obtained samples were donated as Cu@S and $CuFe_{0.5}$@S and the ideal Cu, Fe loading was 5% and 0.5%.

3.3. Catalysts Characterization

The textural properties of different configurational catalysts were measured through N_2 physisorption, which was performed on the Micro-meritics ASAP 2460 instrument. Before the experiment, all samples were degassed under a vacuum for 12 h. The Brunauer-Emmett-Teller (BET) method was applied for calculating the total surface area. The micro- and meso- were calculated via the t-plot method. In addition, the pore volume and average pore sizes of catalysts were calculated through the Barrett-Joyner-Halenda (BJH) model. Powder X-ray diffraction (XRD) patterns were collected on an EMPYREAN powder diffractometer (PANalytical Corporation, Netherland) using Cu K*a* radiation (λ = 0.154 nm) at a scanning rate of 2°/min from 20° to 70°.

The elemental chemical compositions of configurational catalysts were measured using the X-ray Fluorescence (XRF) spectrometer (ZSX-II, Rigaku). The X-ray photoelectron spectroscopy (XPS) characterizations were carried out on a Thermo ESCALAB 250XI spectrometer equipped with an Al K*a* X-ray radiation source and each element was calibrated via C 1s peak at 284.8 eV.

The morphology of all the samples and the dispersion of metal nanoparticles were measured via scanning electron microscopy (SEM) images (HITACHI, S-4800) and transmission electron microscopy (TEM) images (FEI, Tecnai G2 F20), respectively.

The reducibility of samples was characterized through a H_2 temperature programmed reduction (H_2-TPR) method conducted on a Micromeritics AutoChem II 2920 analyzer suited with a thermal conductivity detector (TCD). In total, 100 mg of the catalysts (40~60 mesh) were used in every H_2-TPR experiment. The samples were pretreated at 200 °C for 60 min with Argon (Ar) flow to remove water and other wastes. After that, the samples were heated from room temperature to 900 °C at the rate of 10 °C/min in a 10% H_2-Ar flow (50 mL/min) and the reduced data were recorded with TCD. In addition, the basicity of catalysts was also analyzed in a Micromeritics AutoChem II 2920 chemical adsorption instrument by a CO_2-temperature programmed desorption (CO_2-TPD) method. In this regard, 200 mg of the catalysts (40~60 mesh) were per-reduced at 600 °C for 2 h with H_2. After cooling to 50 °C, the samples were saturated by CO_2 gas with a flowing rate of 50 mL/min followed by sweeping with flowing Ar at the same temperature for 30 min to remove physically adsorbed CO_2. The desorption procedure was carried out between 50 and 800 °C at a rate of 10 °C/min under Ar flow (50 mL/min) and the desorption curve was also recorded with TCD.

3.4. Catalytic Evaluation

The catalytic performance of different configurational catalysts was performed in a fixed-bed quartz reactor (ID = 8 mm) at atmospheric pressure. Typically, 0.5 g of catalyst (40~60 mesh) was mixed with SiO_2 (40~60 mesh) to 5 mL. Then the above mixture was added into the isothermal region of the reactor. All the samples were reduced under a 60% H_2/N_2 flow at the rate of 120 mL min^{-1} at 600 °C for 3 h under atmospheric pressure. After cooling down to room temperature, the reactors were pressurized employing a feed stream with composition of 12 vol% H_2/36 vol% CO_2/52 vol% N_2; the catalytic performance of the catalysts was evaluated at 400–550 °C with the heating rate of 2 °C·min^{-1}. The tail gas was analyzed by the Agilent 9000 B gas chromatograph equipped with a FID detector and a TCD detector. All data points were collected at a steady state after continuously reacting for 2 h. N_2 in the feed gas was assumed an internal standard during the reaction. The conversion and selectivity were calculated via the different equations as follows:

$$X_{CO_2} = \frac{F_{CO_2,in} - F_{CO_2,out}}{F_{CO_2,in}} \times 100\%$$
$$S_{CO} = \frac{F_{CO,out}}{F_{CO_2,in} - F_{CO_2,out}} \times 100\%$$

The "*in*" or "*out*" in the above equation represents gas that flows into or out of the reactor.

4. Conclusions

The hollow hierarchical structure Cu@S and $CuFe_{0.5}$@S catalysts were successfully synthesized through the dissolution recrystallization (D-R) method for the RWGS reaction. The encapsulated catalysts had a hierarchical porous structure and better dispersion of Cu particles compared to the Cu-S and $CuFe_{0.5}$-S catalysts prepared via a conventional impregnation method. Moreover, compared to monometallic Cu-S and Cu@S catalysts, $CuFe_{0.5}$-S and $CuFe_{0.5}$@S catalysts showed a higher CO_2 conversion and 100% selectivity of CO at the entire temperature range investigated in this work as a result of introducing FeO_x species. Furthermore, the reaction activity of all the samples increased according to the sequence: $CuFe_{0.5}$@S > $CuFe_{0.5}$-S > Cu@S > Cu-S at 400–550 °C under atmospheric pressure. The remarkably enhanced catalytic performance in the RWGS reaction was associated with the higher dispersion of encapsulation structure and the enhanced surface basicity derived from the addition of Fe. This work provides some optimistic prospects in designing high-exhibition catalysts for the RWGS reaction and even the utilization of CO_2 hydrogenation.

Author Contributions: Conceptualization, Z.D.; methodology, Y.W. (Yu Wu), E.X. and Z.D.; software, Y.W. (Yifan Wang); investigation, R.H.; resources, T.W., Y.W. (Yifan Wang), E.X., Y.W. (Yu Wu) and Z.D.; data curation, T.W. and F.W.; supervision, E.X., Y.W. (Yu Wu) and Z.D.; project administration, Z.D.; funding acquisition, Z.D., Y.Z. and H.L. All authors have read and agreed to the published version of the manuscript.

Funding: The research was funded by the National Key Research and Development Plan of China (No. 2021YFE0191200-2) and The Science & Technology Foundation of RIPP (PR20230260, 922018).

Conflicts of Interest: The authors declare that they have no known competing financial interest or personal relationship that could have appeared to influence the work reported in this paper.

References

1. Enthaler, S.; von Langermann, J.; Schmidt, T. Carbon dioxide and formic acid—The couple for environmental-friendly hydrogen storage? *Energy Environ. Sci.* **2010**, *3*, 1207–1217. [CrossRef]
2. Ghoniem, A.F. Needs, resources and climate change: Clean and efficient conversion technologies. *Prog. Energy Combust. Sci.* **2011**, *37*, 15–51. [CrossRef]
3. Saeidi, S.; Najari, S.; Hessel, V.; Wilson, K.; Keil, F.J.; Concepción, P.; Suib, S.L.; Rodrigues, A.E. Recent advances in CO_2 hydrogenation to value-added products—Current challenges and future directions. *Prog. Energy Combust. Sci.* **2021**, *85*, 100905. [CrossRef]
4. Pahija, E.; Panaritis, C.; Gusarov, S.; Shadbahr, J.; Bensebaa, F.; Patience, G.; Boffito, D.C. Experimental and Computational Synergistic Design of Cu and Fe Catalysts for the Reverse Water–Gas Shift: A Review. *ACS Catal.* **2022**, *12*, 6887–6905. [CrossRef]
5. González-Castaño, M.; De Miguel, J.N.; Sinha, F.; Wabo, S.G.; Klepel, O.; Arellano-Garcia, H. Cu supported Fe-SiO_2 nanocomposites for reverse water gas shift reaction. *J. CO2 Util.* **2021**, *46*, 101493. [CrossRef]
6. Daza, Y.A.; Kuhn, J.N. CO_2 conversion by reverse water gas shift catalysis: Comparison of catalysts, mechanisms and their consequences for CO_2 conversion to liquid fuels. *RSC Adv.* **2016**, *6*, 49675–49691. [CrossRef]
7. Jurković, D.L.; Prašnikar, A.; Pohar, A.; Likozar, B. Surface structure-based CO_2 reduction reaction modelling over supported copper catalysts. *J. CO2 Util.* **2020**, *41*, 101234. [CrossRef]
8. Vogt, C.; Groeneveld, E.; Kamsma, G.; Nachtegaal, M.; Lu, L.; Kiely, C.J.; Berben, P.H.; Meirer, F.; Weckhuysen, B.M. Unravelling structure sensitivity in CO_2 hydrogenation over nickel. *Nat. Catal.* **2018**, *1*, 127–134. [CrossRef]
9. Chen, C.-S.; Cheng, W.-H.; Lin, S.-S. Study of iron-promoted Cu/SiO_2 catalyst on high temperature reverse water gas shift reaction. *Appl. Catal. A Gen.* **2004**, *257*, 97–106. [CrossRef]
10. Joo, O.-S.; Jung, K.-D.; Moon, I.; Rozovskii, A.Y.; Lin, G.I.; Han, S.-H.; Uhm, S.-J. Carbon Dioxide Hydrogenation To Form Methanol via a Reverse-Water-Gas-Shift Reaction (the CAMERE Process). *Ind. Eng. Chem. Res.* **1999**, *38*, 1808–1812. [CrossRef]
11. Yang, H.; Gao, P.; Zhang, C.; Zhong, L.; Li, X.; Wang, S.; Wang, H.; Wei, W.; Sun, Y. Core–shell structured Cu@m-SiO_2 and Cu/ZnO@m-SiO_2 catalysts for methanol synthesis from CO_2 hydrogenation. *Catal. Commun.* **2016**, *84*, 56–60. [CrossRef]
12. Zeng, B.; Hou, B.; Jia, L.; Wang, J.; Chen, C.; Li, D.; Sun, Y. The intrinsic effects of shell thickness on the Fischer–Tropsch synthesis over core–shell structured catalysts. *Catal. Sci. Technol.* **2013**, *3*, 3250–3255. [CrossRef]
13. Prieto, G.; Tüysüz, H.; Duyckaerts, N.; Knossalla, J.; Wang, G.-H.; Schüth, F. Hollow Nano- and Microstructures as Catalysts. *Chem. Rev.* **2016**, *116*, 14056–14119. [CrossRef]
14. Wu, S.M.; Yang, X.Y.; Janiak, C. Confinement Effects in Zeolite-Confined Noble Metals. *Angew. Chem. Int. Ed.* **2019**, *58*, 12340–12354. [CrossRef] [PubMed]

15. Kwok, K.M.; Ong, S.W.D.; Chen, L.; Zeng, H.C. Transformation of Stöber Silica Spheres to Hollow Hierarchical Single-Crystal ZSM-5 Zeolites with Encapsulated Metal Nanocatalysts for Selective Catalysis. *ACS Appl. Mater. Interfaces* **2019**, *11*, 14774–14785. [CrossRef] [PubMed]
16. Liu, Y.; Chen, Y.; Gao, Z.; Zhang, X.; Zhang, L.; Wang, M.; Chen, B.; Diao, Y.; Li, Y.; Xiao, D.; et al. Embedding high loading and uniform Ni nanoparticles into silicalite-1 zeolite for dry reforming of methane. *Appl. Catal. B Environ.* **2022**, *307*, 121202. [CrossRef]
17. Zhang, F.; Zhou, W.; Xiong, X.; Wang, Y.; Cheng, K.; Kang, J.; Zhang, Q.; Wang, Y. Selective Hydrogenation of CO_2 to Ethanol over Sodium-Modified Rhodium Nanoparticles Embedded in Zeolite Silicalite-1. *J. Phys. Chem. C* **2021**, *125*, 24429–24439. [CrossRef]
18. Dai, C.; Zhang, A.; Luo, L.; Zhang, X.; Liu, M.; Wang, J.; Guo, X.; Song, C. Hollow zeolite-encapsulated Fe-Cu bimetallic catalysts for phenol degradation. *Catal. Today* **2017**, *297*, 335–343. [CrossRef]
19. Zhu, C.; Zhang, M.; Huang, C.; Han, Y.; Fang, K. Controlled Nanostructure of Zeolite Crystal Encapsulating FeMnK Catalysts Targeting Light Olefins from Syngas. *ACS Appl. Mater. Interfaces* **2020**, *12*, 57950–57962. [CrossRef]
20. Niu, X.; Li, X.; Yuan, G.; Feng, F.; Wang, M.; Zhang, X.; Wang, Q. Hollow Hierarchical Silicalite-1 Zeolite Encapsulated PtNi Bimetals for Selective Hydroconversion of Methyl Stearate into Aviation Fuel Range Alkanes. *Ind. Eng. Chem. Res.* **2020**, *59*, 8601–8611. [CrossRef]
21. Fu, T.; Qi, R.; Wang, X.; Wan, W.; Li, Z. Facile synthesis of nano-sized hollow ZSM-5 zeolites with rich mesopores in shell. *Microporous Mesoporous Mater.* **2017**, *250*, 43–46. [CrossRef]
22. Wang, Y.; Lin, M.; Tuel, A. Hollow TS-1 crystals formed via a dissolution–recrystallization process. *Microporous Mesoporous Mater.* **2007**, *102*, 80–85. [CrossRef]
23. Wei, F.-F.; Liu, J.; Zhang, Q.-Y.; Zhang, Y.-T.; Zhang, X.; Cao, C.-Y.; Song, W.-G. Sharp size-selective catalysis in a liquid solution over Pd nanoparticles encapsulated in hollow silicalite-1 zeolite crystals. *RSC Adv.* **2016**, *6*, 89499–89502. [CrossRef]
24. Dai, C.; Zhang, A.; Liu, M.; Guo, X.; Song, C. Hollow ZSM-5 with Silicon-Rich Surface, Double Shells, and Functionalized Interior with Metallic Nanoparticles and Carbon Nanotubes. *Adv. Funct. Mater.* **2015**, *25*, 7479–7487. [CrossRef]
25. Bergeret, G.; Gallezot, P. Particle Size and Dispersion Measurements. In *Handbook of Heterogeneous Catalysis*; Wiley: Hoboken, NJ, USA, 2008; pp. 738–765.
26. Liu, G.; Tian, Y.; Zhang, B.; Wang, L.; Zhang, X. Catalytic combustion of VOC on sandwich-structured Pt@ZSM-5 nanosheets prepared by controllable intercalation. *J. Hazard. Mater.* **2019**, *367*, 568–576. [CrossRef]
27. Chen, C.-S.; Cheng, W.-H.; Lin, S.-S. Enhanced activity and stability of a Cu/SiO_2 catalyst for the reverse water gas shift reaction by an iron promoter. *Chem. Commun.* **2001**, *18*, 1770–1771. [CrossRef]
28. Li, S.; Tuel, A.; Laprune, D.; Meunier, F.; Farrusseng, D. Transition-Metal Nanoparticles in Hollow Zeolite Single Crystals as Bifunctional and Size-Selective Hydrogenation Catalysts. *Chem. Mater.* **2014**, *27*, 276–282. [CrossRef]